Monthly Notices
of the
ROYAL ASTRONOMICAL SOCIETY

MNRAS **465,** 1831–1846 (2017)
Advance Access publication 2016 October 26

doi:10.1093/mnras/stw2741

The SDSS-IV eBOSS: emission line galaxy catalogues at $z \approx 0.8$ and study of systematic errors in the angular clustering

T. Delubac,[1⋆] A. Raichoor,[2] J. Comparat,[3,4] S. Jouvel,[5] J.-P. Kneib,[1,6] C. Yèche,[2] H. Zou,[7] J. R. Brownstein,[8] F. B. Abdalla,[5,9] K. Dawson,[8] E. Jullo,[6] A. D. Myers,[10] J. A. Newman,[11] W. J. Percival,[12] F. Prada,[4,13,14] A. J. Ross,[12,15] D. P. Schneider,[16,17] X. Zhou,[7] Z. Zhou[7] and G. Zhu[18]

Affiliations are listed at the end of the paper

Accepted 2016 October 21. Received 2016 September 18; in original form 2015 December 21

ABSTRACT

We present two wide-field catalogues of photometrically selected emission line galaxies (ELGs) at $z \approx 0.8$ covering about 2800 deg^{2}over the south galactic cap. The catalogues were obtained using a Fisher discriminant technique described in a companion paper. The two catalogues differ by the imaging used to define the Fisher discriminant: the first catalogue includes imaging from the Sloan Digital Sky Survey and the *Wide-field Infrared Survey Explorer*, the second also includes information from the South Galactic Cap *U*-band Sky Survey. Containing respectively 560 045 and 615 601 objects, they represent the largest ELG catalogues available today and were designed for the ELG programme of the extended Baryon Oscillation Spectroscopic Survey (eBOSS). We study potential sources of systematic variation in the angular distribution of the selected ELGs due to fluctuations of the observational parameters. We model the influence of the observational parameters using a multivariate regression and implement a weighting scheme which allows effective removal of all of the systematic errors induced by the observational parameters. We show that fluctuations in the imaging zero-points of the photometric bands have minor impact on the angular distribution of objects in our catalogues. We compute the angular clustering of both catalogues and show that our weighting procedure effectively removes spurious clustering on large scales. We fit a model to the small-scale angular clustering, showing that the selections have similar biases of $1.35/D_a(z)$ and $1.28/D_a(z)$. Both catalogues are publicly available.

Key words: methods: data analysis – catalogues – galaxies: distances and redshifts – galaxies: general – galaxies: photometry – cosmology: observations.

1 INTRODUCTION

The development of large-scale spectroscopic surveys such as the Sloan Digital Sky Survey (SDSS; York et al. 2000) and the 2-degree Field Galaxy Redshift Survey (Colless et al. 2001) set a milestone in the era of precision cosmology by allowing the first detection of baryon acoustic oscillations (BAO) in the power spectrum of the galaxy density field (Cole et al. 2005; Eisenstein et al. 2005). The Baryon Oscillation Spectroscopic Survey (BOSS; Dawson et al. 2013), one of the experiments of the third generation of the SDSS (SDSS-III; Eisenstein et al. 2011), recently produced 1–2 per cent precision measurements of the BAO scale for redshifts $z < 0.6$ using a total of about 1.3 million luminous red galaxies (LRGs; Anderson et al. 2014; Tojeiro et al. 2014). It also produced a 2 per cent measurement of the BAO scale at redshift 2.34 (Font-Ribera et al. 2014; Delubac et al. 2015) using the Lyman alpha forests of nearly 140 000 quasars. These results, combined with cosmic microwave background (CMB; Planck Collaboration XVI 2014) and supernova measurements (e.g. Betoule et al. 2014), yielded tight constraints on cosmological parameters such as the dark energy and dark matter densities, the dark energy equation of state, the Hubble parameter H_0 and the sum of neutrino masses m_ν (Aubourg et al. 2015).

Building on the success of BOSS, the extended Baryon Oscillation Spectroscopic Survey (eBOSS; Dawson et al. 2016) will further tighten the current constraints on cosmological parameters by measuring the BAO scale at several redshifts in the currently unprobed range of $0.7 < z < 2.0$. This will be achieved by targeting LRGs up to redshift 1.0 but also by using two new tracers of the matter

⋆ E-mail: timothee.delubac@epfl.ch

density field: quasar in the redshift range $0.9 < z < 2.0$ and emission line galaxies (ELGs) in the redshift range $0.6 < z < 1.1$. eBOSS will provide the first 2 per cent measurement of the BAO scale using ELGs as a tracer (Zhao et al. 2016). This measurement will pave the way for future experiments such as the Dark Energy Spectroscopic Instrument[1] (Levi et al. 2013), the 4-metre Multi-Object Spectroscopic Telescope[2] (de Jong et al. 2014), the space mission *Euclid*[3] (Laureijs et al. 2011) of the European Space Agency and the Subaru Prime Focus Spectrograph[4] (Takada et al. 2014) which will all use ELGs as a main tracer of the matter density field. eBOSS uses the same facility as BOSS, including the 2.5 m Sloan telescope (Gunn et al. 2006), the two fibre-fed spectrographs (Smee et al. 2013) as well as an upgraded version of the BOSS pipeline (Bolton et al. 2012).

The development of large spectroscopic surveys is tightly coupled to the development of large photometric surveys such as the imaging programme of the SDSS (Gunn et al. 1998; York et al. 2000) and the Canada–France–Hawaii Telescope Legacy Survey (Gwyn 2012). Large and homogeneous photometric data sets are a requirement for the selection of spectroscopic targets. Since the early stages of the SDSS it has been recognized that inhomogeneities in the imaging data sets used for the target selection (e.g. due to variation of the seeing or sky flux) or astrophysical parameters such as the stellar density and Galactic extinction could induce artificial fluctuations in the target density and produce systematic errors in clustering measurements such as the angular or three-dimensional correlation functions (see e.g. Scranton et al. 2002; Myers et al. 2006; Ross et al. 2011; Ho et al. 2012).

In this paper, we present two large-scale catalogues of $z \approx 0.8$ ELGs selected by their photometry using a Fisher discriminant technique (Fisher 1936). The information used to produce the catalogues includes SDSS *griz* photometric bands, the *Wide-field Infrared Survey Explorer*[5] (*WISE*) 3.4 μm *W*1 band as well as the South Galactic Cap *U*-band Sky Survey[6] (SCUSS) *U* band. The selection algorithm as well as preliminary spectroscopic results obtained by eBOSS dedicated observations are presented in a companion paper (Raichoor et al. 2016, hereafter R16). The paper is structured as follows. Section 2 lists the requirements to produce a catalogue of ELGs suitable for a 2 per cent measurement of the BAO scale. Section 3 presents the photometry used to produce the catalogue and summarize the target selection algorithm and give information on how to access the catalogues. Section 4 describes a study of the impact of observational parameters (such as sky flux or seeing) and astrophysical parameters (such as stellar number densities or extinction) on the angular distribution of ELGs in our catalogue. We use a multivariate regression to accurately model the fluctuations in the angular number density of ELGs induced by those parameters and propose a weighting procedure to remove them. Section 5 presents the large-scale angular clustering of our catalogues and show that our weighting procedure successfully removes spurious clustering on large scales. In Section 6, we compute and model the small-scale angular clustering of both catalogues and measure their biases. We conclude in Section 7.

[1] http://desi.lbl.gov/
[2] https://www.4most.eu/
[3] http://sci.esa.int/euclid/
[4] http://sumire.ipmu.jp/en/
[5] http://wise.ssl.berkeley.edu/
[6] http://batc.bao.ac.cn/Uband/

All magnitudes in this paper are given in the AB system (Oke & Gunn 1983) and, unless stated otherwise, are corrected for Galactic extinction using dusts maps of Schlegel, Finkbeiner & Davis (1998). We consider a flat Λ cold dark matter cosmology with $h = 0.673$, $\Omega_m h^2 = 0.142$, $\Omega_b h^2 = 0.022$, $\sigma_8 = 0.829$, $n_s = 0.96$ (Planck Collaboration XVI 2014) and a CMB temperature of 2.72 K. Coordinates are given in the J2000 equatorial system.

2 COSMOLOGICAL GOALS AND IMPLICATIONS FOR TARGET SELECTION

The primary goal of the eBOSS ELG survey is to produce the first 2 per cent measurements of the BAO scale and redshift space distortion using ELGs as a tracer of the underlying matter density field. Constraints and requirements regarding the ELG survey are presented in eBOSS overview paper, Dawson et al. (2016), while forecasts about cosmological results are given in Zhao et al. (2016). Approximately 300 eBOSS plates will be dedicated to the ELG survey. The minimum surface density which can be efficiently tiled for the ELG programme is 170 deg^{-2}; thus, the targets should be contained within a footprint of 1500 deg^2. The final spectroscopic sample should contain classification of 190 000 ELGs, corresponding to a sample purity of 74 per cent. The width of the redshift distribution of the ELG sample should be less than $\Delta z = 0.4$ and contained in the redshift range $0.6 < z < 1.0$ or $0.7 < z < 1.1$.

To ensure that our clustering analysis and cosmological measurements will be limited by statistical uncertainties, we further impose a list of requirements on our target sample which limit the systematic uncertainties. The requirements are derived from knowledge of the BOSS survey and are fully explained in Dawson et al. (2016). We summarize the principal points below.

(i) The redshift uncertainty should be below 300 km s^{-1} rms at all redshifts.
(ii) Catastrophic redshift errors (i.e. error exceeding 1000 km s^{-1} and without knowledge that the redshift is wrongly estimated) should be below 1 per cent.
(iii) We require that the maximum absolute variation in expected galaxy density as a function of flux limit, stellar density and Galactic extinction be less than 15 per cent within the survey footprint.
(iv) We require that the maximum absolute variation in expected galaxy density as a function of imaging zero-point be less than 15 per cent within the survey footprint.

Comparat et al. (2016) studied in detail the accuracy and catastrophic errors of ELG redshift assignment with eBOSS pipeline. The typical redshift accuracy is of the order of 30 km s^{-1}, well below the requirement, and the catastrophic redshift fraction is lower than 1 per cent. R16 proposed two selections, both using a Fisher discriminant technique, which satisfy the target density, the redshift distribution, as well as the purity requirements. They developed the selection on a ≈50 deg^2 area and evaluated it using dedicated eBOSS test plates. In this paper, we investigate if these two selections, the *UgrizW* and *griW* selections, pass the remaining homogeneity requirements on large scales. In addition, we identify the dominant sources of systematic errors and investigate ways of correcting for them.

3 PARENT IMAGING AND TARGET SELECTION

The *UgrizW* and *griW* selections both use combined information from different photometric catalogues. The *griW* selection uses

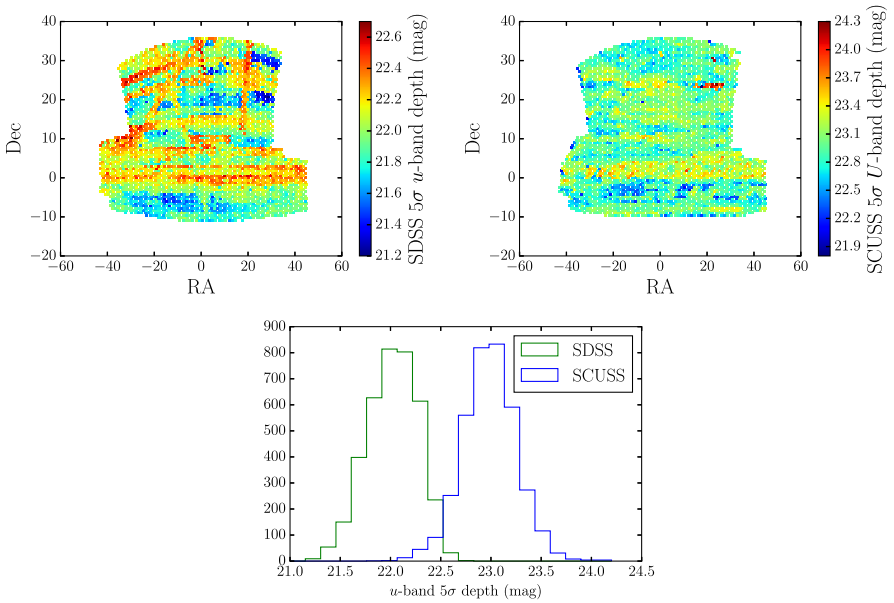

Figure 1. Upper left: 5σ limiting magnitude maps of the SDSS SGC in the u band. Upper right: 5σ limiting magnitude maps of SCUSS U band. Both maps are divided into equal-area pixels of 0.84 deg^2 (HEALPIX NSIDE = 64). Bottom: histogram of the 5σ limiting magnitude per pixel of SCUSS U band (blue) and SDSS u band (green). This histogram shows that the SCUSS survey is about 1 mag deeper than the SDSS u band.

SDSS g, r and i bands as well as *WISE* infrared $W1$ information, while the *UgrizW* also includes SDSS z band as well as SCUSS U band. This section introduces the different photometric catalogues used as well as the algorithms defining the selections.

3.1 SDSS imaging

The SDSS is the principal imaging data set used for our selections with all ELG targets being detected in SDSS images (while SCUSS and *WISE* counterparts are derived from forced photometry). These images were obtained during the three first stages of the SDSS (I/II/III) using a wide-field imager (Gunn et al. 1998) mounted on the SDSS 2.5 m telescope (Gunn et al. 2006). Images were taken in the *ugriz* system described in Fukugita et al. (1996). The 95 per cent detection repeatability for point sources of SDSS imaging has been estimated on the early data release of the SDSS to be on average $u = 22.0$, $g = 22.2$, $r = 22.2$, $i = 21.3$ and $z = 20.5$ (Stoughton et al. 2002). However, those results are given in luptitudes (Lupton, Gunn & Szalay 1999), and the south galactic cap (SGC) is not representative of the SDSS imaging as it is more contaminated by observational parameters such as extinction, which is on average higher than in the north galactic cap (NGC), and the airmass, which is higher for the SGC (at low declination). Accurate knowledge of the depth of the catalogue is important as the targets are high-redshift galaxies and thus likely to reach the faint end of the catalogue. To produce depth maps for each SDSS band, we divide the SGC into equal-area pixels using the HEALPIX package[7] (Gorski et al. 1999) with NSIDE set to 64 corresponding to pixels of 0.84 deg^2. For each pixel, we select point-like objects (using SDSS flag TYPE = 6) which have a signal-to-noise ratio for the psfMag[8] between 4 and 6. We then draw the histogram of the psfMag (uncorrected for extinction) of the objects in a given pixel and report the maximum of the histogram as the limiting magnitude. The resulting map for the u band is shown in Fig. 1. The 5th percentile of the distributions of the limiting magnitude per pixel over the SGC footprint is, respectively, $u = 21.6$, $g = 22.8$, $r = 22.3$, $i = 21.8$ and $z = 20.4$. In the following, unless otherwise stated, we consider modelMag[9] magnitudes corrected for Galactic extinction for the SDSS photometric bands.

3.2 SCUSS imaging

The SCUSS (Zou et al. 2015, 2016) is an international project undertaken by the National Astronomical Observatories of China (Chinese Academy of Sciences) and the Steward Observatory (University of Arizona). It is a U-band ($\sim$3540 Å) survey which used the Bok 2.3 m telescope to cover about 5000 deg^2 of the SGC, 80 per cent of which overlaps the SDSS footprint. We use a forced-photometry catalogue based on SDSS detections and, for each object, measure SCUSS modelMag using SDSS model to ensure consistent photometric measurements between SDSS and SCUSS. We estimate the SCUSS 5σ detection depth using the same technique as previously. The resulting map, together with the histogram of magnitude limit per pixel, is shown in Fig. 1. Also presented is the histogram of the magnitude limit per pixel for SDSS u band, which demonstrates that SCUSS is on average 1 mag deeper than SDSS u band. This deeper U-band imaging is especially useful because the [O II] flux strength of ELGs correlates with the u-band magnitude (Comparat et al. 2015).

3.3 *WISE* imaging

The *WISE* (Wright et al. 2010) is a full-sky survey in four mid-infrared wavelength filters labelled $W1$ to $W4$ centred at 3.4, 4.6, 12 and 22 μm. We use the forced-photometry catalogue of Lang, Hogg & Schlegel (2016), where *WISE* photometry is derived using

[7] http://healpix.jpl.nasa.gov/
[8] https://www.sdss3.org/dr10/algorithms/magnitudes.php#mag_psf
[9] https://www.sdss3.org/dr10/algorithms/magnitudes.php#mag_model

Table 1. The *griW* and *UgrizW* selection criteria for the catalogues in this paper. $\mathrm{err_X}$ corresponds to the estimated error on the magnitude *X*. For an extensive discussion on how those cuts were defined, we refer the reader to R16.

	griW	*UgrizW*
Photometric data sets	SDSS *gri* *WISE W1*	SCUSS *u* SDSS *griz* *WISE W1*
$X_{\rm FI}$ param.	$\alpha_0 = +0.104$ $\alpha_{ur} = 0$ $\alpha_{gr} = -1.308$ $\alpha_{ri} = +0.870$ $\alpha_{rz} = 0$ $\alpha_{rW1} = +0.782$	$\alpha_0 = +0.956$ $\alpha_{ur} = -0.650$ $\alpha_{gr} = -0.781$ $\alpha_{ri} = +0.065$ $\alpha_{rz} = +0.229$ $\alpha_{rW1} = +0.739$
$X_{\rm FI}$ cut	$X_{\rm FI} > 1.49$	$X_{\rm FI} > 1.16$
Magnitude cuts	$20.0 < g < 22.5$, $\mathrm{err}_g < 0.5$ $19.0 < r < 22.5$, $\mathrm{err}_r < 0.5$ $19.0 < i < 21.5$, $\mathrm{err}_i < 0.5$ $17.0 < W1 < 21.0$, $\mathrm{err}_{W1} < 0.5$	$20.0 < u < 23.5$, $\mathrm{err}_u < 1.0$ $20.0 < g < 22.5$, $\mathrm{err}_g < 0.5$ $19.0 < r < 22.5$, $\mathrm{err}_r < 0.5$ $19.0 < i < 21.5$, $\mathrm{err}_i < 0.5$ $17.0 < W1 < 21.0$, $\mathrm{err}_{W1} < 0.5$
Other cuts	`BINNED2` $= 0$ `OBJC_TYPE` $= 3$ or $r > 22$ Bright stars masked	

SDSS detections and galaxy profiles. As shown in R16, the use of *WISE* imaging allows efficient removal of low-redshift galaxies and can distinguish between $0.6 \lesssim z_{\rm spec} \lesssim 1.0$ LRGs and ELGs. We only consider the *W*1 band as it has the highest signal-to-noise ratio and as we found that including *W*2 band introduces spurious fluctuations in the density map likely due to Moon patterns in the *W*2 photometry.

3.4 Selection algorithm

The method used to select ELGs is extensively described in the companion paper R16. It consists of a Fisher discriminant technique applied to a set of colour measurements including SDSS *griz*-band, SCUSS *U*-band and *WISE W*1-band information. The Fisher discriminant quantity $X_{\rm FI}$ is defined as

$$X_{\rm FI} = \alpha_0 + \alpha_{ur} \times (u - r) + \alpha_{gr} \times (g - r) + \alpha_{ri} \times (r - i) + \alpha_{rz} \times (r - z) + \alpha_{rW1} \times (r - W1), \quad (1)$$

where the values of α are optimized using training samples so that ELGs in the redshift range of interest receive a high value of $X_{\rm FI}$ while other objects such as stars or galaxies outside the redshift range are assigned a small value of $X_{\rm FI}$. Thus, a given Fisher selection is defined by a set of α parameters plus a lower cut on $X_{\rm FI}$. R16 proposed two possible discriminants which satisfy eBOSS target selection requirements in terms of mean redshift, observation completeness, redshift accuracy and catastrophic redshift errors (those two last points being discussed in detail in Comparat et al. 2016). The first selection is restricted to SDSS *gri* bands and *WISE W*1 band, and is referred to as the *griW* selection. The second option includes information from the SDSS *z* band and SCUSS *U* band and is referred to as the *UgrizW* selection. We summarize the main characteristics of both selections in Table 1[10] and refer the reader to R16 for a detailed discussion on the selections.

[10] The cut on the Fisher discriminant of the *UgrizW* selection is slightly lower than the one used in R16. This difference is due to the fact that the selection was optimized on a low-extinction region on which the mean density of the selection is higher than on the full SGC. The cut was lowered to recover an average mean density greater than 180 deg^{-2} over the full SGC.

3.5 Accessing the catalogue

The *UgrizW* and *griW* catalogues are publicly available.[11] The catalogues include for each object position and photometric information as well as estimates of the correction weight defined in Section 4.4 for clustering analysis. Though we do not study systematics on the NGC in this paper, the public version of the *griW* selection also includes objects selected on the NGC, corresponding to 1440 750 more objects. The *UgrizW* catalogue does not contain object over the NGC as no SCUSS information is available on that region. A full description of the catalogues is available on the SDSS website.[12]

4 SYSTEMATIC EFFECTS ON THE ANGULAR DISTRIBUTION OF GALAXIES

4.1 Observational parameters

The *griW* and *UgrizW* catalogues are cleaned using standard SDSS Mangle (Swanson et al. 2008) masks for bright stars, bright objects and bad photometry (`bright_stars`, `badfield`, `bad_objects`),[13] as well as an additional mask intended to remove bright stars surroundings in *WISE* photometry. The latter is a custom mask which was developed after finding overdensities in our selection in the vicinity of bright stars. These overdensities resulted from the overestimation of *WISE W*1 fluxes in the halo of bright stars on radii significantly larger than the one removed by SDSS masks. In its current implementation, described in R16, this custom mask removes about 100 deg^2 over the SGC. This estimate is conservative, and in the future a more careful estimation of the span of *W*1 bright star haloes could reduce the masked area.

After applying masks, we divide our maps into equal-area pixels of $\approx$0.21 deg^2 (corresponding to `HEALPIX NSIDE = 128`), and compute the number density in each pixel. The resulting maps are

[11] https://data.sdss.org/sas/dr13/eboss/target/elg/fisher-selection/

[12] https://data.sdss.org/datamodel/files/EBOSS_TARGET/elg/fisher-selection/

[13] http://data.sdss3.org/sas/dr10/boss/lss/reject_mask/

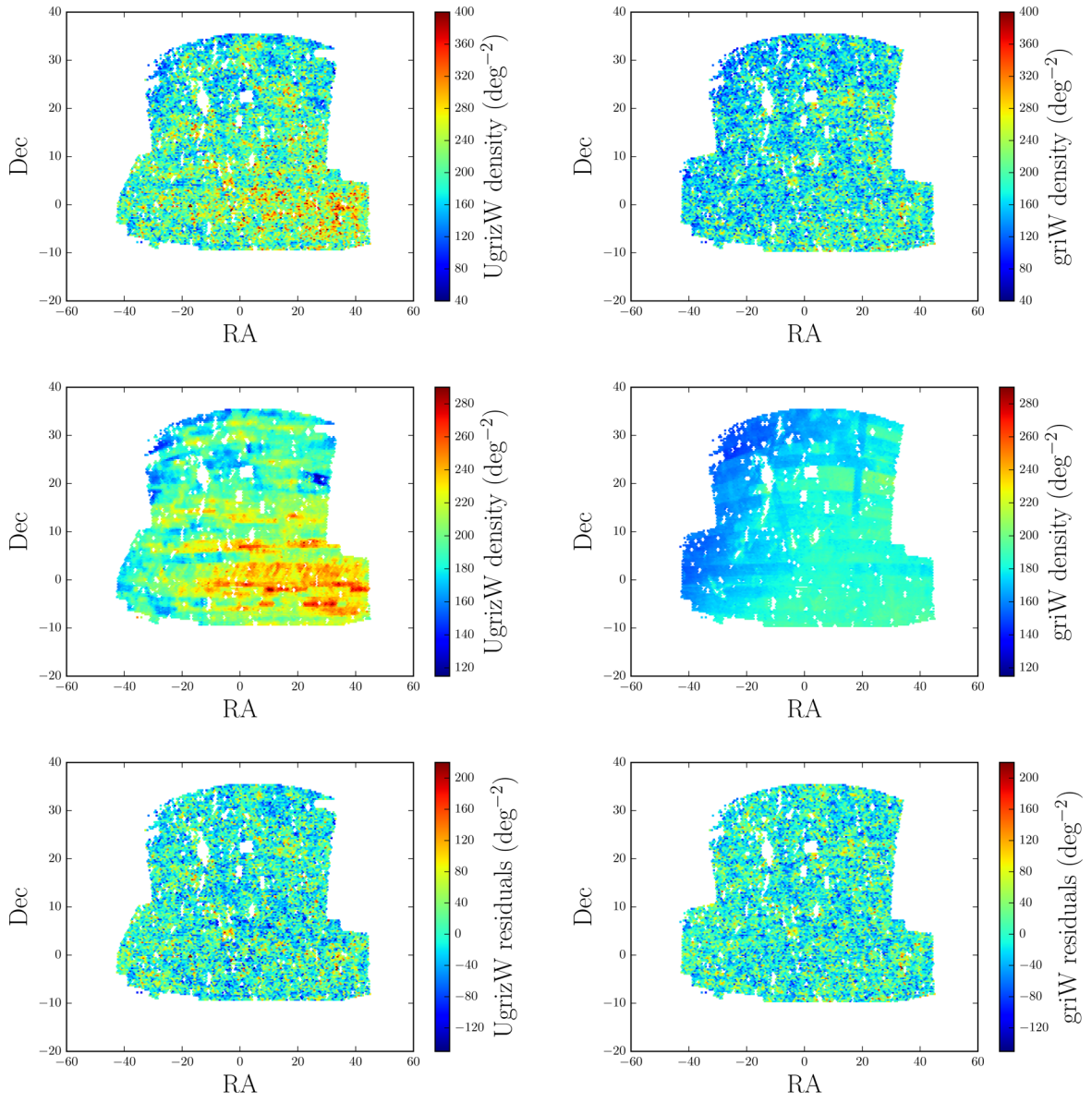

Figure 2. Top row: density maps of the *UgrizW* (left) and *griW* (right) selections. The maps are divided into equal-area pixels of 0.21 deg^2 (HEALPIX NSIDE = 128). The holes in the footprint correspond to masked regions. Middle row: predicted density maps for the *UgrizW* (left) and *griW* (right) selections obtained using the multivariate regression defined in Section 4.3. The good agreement with the original density maps is clearly visible as higher density regions in the selection density maps correspond to high-density regions in the predicted density maps. We emphasize that the colour scales of the *griW* and *UgrizW* maps are the same, clearly demonstrating that the *griW* predicted density is more homogeneous than the *UgrizW* one. Bottom row: residual maps for the *UgrizW* (left) and *griW* (right) selections obtained by subtracting the predicted densities to the selection densities.

shown in the top row of Fig. 2. The choice of the size of the pixels is a compromise between the necessity of having sufficiently small pixels to have a precise estimation of the observational parameters and the requirement of having sufficiently large pixels such that we do not have to deal with empty pixels and that the shot noise can be approximated as Gaussian. We also require that the pixel size be smaller than the BAO scale of $2\overset{\circ}{.}99$ in our fiducial cosmology for $z = 0.8$. We compute the effective area of each pixel by accounting for area covered by the different masks. We remove every pixel which has more than 20 per cent of its area masked and otherwise correct the density by the amount of unmasked area.

For both the *griW* and *UgrizW* selections, we consider the following observational parameters as potentially impacting the angular distribution of galaxies.

(i) $n_{\rm stars}$: the number density of SDSS TYPE = 6 objects (point sources) satisfying $18 < g < 21$, where g corresponds to a point spread function magnitude not corrected for Galactic extinction. We select stars in the g band to be consistent with our g-band limited selections, but without going as deep as 22.5 as morphological information is not reliable at that level. We also cut on the CLEAN flag[14] to include only secure photometric detections.

(ii) A_g: g-band extinction derived from Schlegel et al. (1998) Galactic extinction maps and converted into magnitudes using the relation $A_g = 3.303E(B - V)$ (Dawson et al. 2016).

(iii) airmass$_{\rm SDSS}$: SDSS airmass in the g band.

[14] https://www.sdss3.org/dr8/algorithms/photo_flags_recommend.php

Table 2. Observational parameters studied for the two selections. The *Survey* column indicates to what survey the parameter is relevant. The *Cut* column provides, when relevant, the cuts applied for the analysis. The $\bar{s}_i$ and σ_{s_i} columns, respectively, list the mean and the standard deviation of the value of the observational parameters in the analysis pixels. The *Model* column indicates whether the modelling of the parameter in equation (3) is quadratic (Q) or linear (L). Parameters marked with a † symbol are only considered for the *UgrizW* selection.

Obs. parameter	Survey	unit	Cut	$\bar{s}_i$	σ_{s_i}	Model
$n_{\rm stars}$	all	deg^{-2}	<6000	1.9e3	1.1e3	Q
A_g	all	mag	<0.5	0.19	0.085	Q
sky$_{\rm SDSS}$	SDSS	nMgy arcsec^{-2}	<2.4	1.6	0.25	Q
airmass$_{\rm SDSS}$	SDSS	–	–	1.3	0.19	L
seeing$_{\rm SDSS}$	SDSS	arcsec	–	1.3	0.18	L
covmedian	*WISE*	–	–	28	5.4	L
seeing$_{\rm SCUSS}$†	SCUSS	mag	–	1.9	0.40	L
sky$_{\rm SCUSS}$†	SCUSS	mag	–	22	2.2	L

(iv) sky$_{\rm SDSS}$: SDSS sky flux[15] in the g band in nMgy arcsec^{-2}.

(v) seeing$_{\rm SDSS}$: SDSS full width at half-maximum seeing in arcsec.

(vi) covmedian: *WISE* median number of single-exposure frames per pixel.

For the *UgrizW* selection, we consider the following additional parameters.

(i) sky$_{\rm SCUSS}$: SCUSS sky flux in magnitude.

(ii) seeing$_{\rm SCUSS}$: SCUSS seeing in arcsec.

All of those observational parameters are summarized in Table 2.

We estimate the value of the observational parameters in the same pixels used to compute the selection densities (i.e. `NSIDE` = 128). The resulting maps are displayed in Figs 3 and 4. Those figures also show the evolution of the normalized number density ($n/\bar{n}$) as a function of the different observational parameters for the two selections. Both the *griW* and *UgrizW* normalized number densities exhibit similar non-linear dependences on stellar density, extinction and SDSS sky flux. To contain the propagation of errors due to those parameters, we discard pixels with $n_{\rm star} > 6000$, $A_g > 0.5$ and sky$_{\rm SDSS}$ >2.4, removing a total of 12 per cent of the initial area.

The stellar density $n_{\rm stars}$ has a strong systematic effect on both selections, with the selection densities dropping by 15–20 per cent when the stellar density increases from 1000 to 5000 deg^{-2}. One usually expects the density of the selection to increase with increasing stellar density due to the stellar contamination of the sample (i.e. stars being erroneously selected as potential ELGs). Actually, as shown by Ross et al. (2011, hereafter ROSS11), the stellar density field also has an opposite effect: due to observational effects (including the seeing and the point spread function of the telescope), each star is observed as a slightly extended object, masking a small fraction of the sky and preventing the selection of galaxies in that region. The negative slope seen in Fig. 3 indicates that this latter effect is dominant for both selections. We conduct a quantitative study of the area masked by foreground stars in Section 4.2.

The Galactic extinction A_g also has a strong effect on the *UgrizW* selection density, which decreases by about 20 per cent as the extinction increases from 0.05 to 0.35 mag. The effect of the extinction on the *griW* selection is weaker: it is contained within 8 per cent over the same range. This effect is expected as over high-extinction regions, the observed flux of our targets is closer to the limiting magnitude of detection, making them harder to select.

The sky$_{\rm SDSS}$ has a relatively weak effect on both selections, with the fluctuations in number densities being contained below 8 per cent for the *griW* selection and below 5 per cent for the *UgrizW*, between 1.3 and 2.0 nMgy arcsec^{-2} which corresponds to 80 per cent of our masked footprint.

The systematic effects induced by the airmass$_{\rm SDSS}$ are comparable to the effects linked to the sky$_{\rm SDSS}$ as the two maps are highly correlated. The effect on the *griW* selection corresponds to a linear increase of about 7 per cent over the range 1.1–1.7; this corresponds to 85 per cent of our masked footprint. The airmass$_{\rm SDSS}$ has essentially no effect on the *UgrizW* selection density.

The impact of the seeing is quite different on the two selections. The variation of densities of the *griW* selection as a function of SDSS seeing is contained within 5 per cent over the full masked footprint. As expected, there is no variation as a function of SCUSS seeing. The *UgrizW* selection density, however, exhibits a strong correlation with both SDSS and SCUSS seeings. The selection density drops by 20 per cent over the range 1.05–1.6 arcsec, which includes more than 90 per cent of the survey. The correlation with SCUSS seeing is opposite and even stronger as the density of the selection increases by 30 per cent over the range 1.2–2.8. This tight correlation between the *UgrizW* selection density and SDSS and SCUSS seeing is due to correlations between those seeing parameters and the colour of objects in our catalogue. Fig. 5 presents the distribution of the pixels in two-dimensional histograms with the mean $U - r$ colour of the objects in a pixel on the y-axis and the seeing on the x-axis. The $U - r$ colour term has a positive correlation with SDSS seeing, whereas it has a negative correlation with SCUSS seeing. This colour term enters the Fisher discriminant $X_{\rm FI}$ of equation (1) multiplied by a negative parameter given in Table 1. A higher value of SDSS seeing implies on average a higher value of $U - r$, thus a lower value of $X_{\rm FI}$: fewer objects will be selected. Conversely, a higher value of SCUSS seeing produces on average a lower value of $U - r$, thus a higher value of $X_{\rm FI}$: more objects will be selected.

The *UgrizW* selection has a 15 per cent variation of density as a function of *WISE* median coverage over the range 22–40 which includes more than 95 per cent of our masked footprint. The effect of covmedian is smaller on the *griW* selection density as the effect is contained within 10 per cent over the full range of values of the observational parameter.

The *UgrizW* selection density is slightly anti-correlated with SCUSS sky flux, exhibiting a 10 per cent decrease over the range 21.2–22.5, which covers 90 per cent of the footprint.

[15] https://www.sdss3.org/dr10/algorithms/magnitudes.php#nmgy

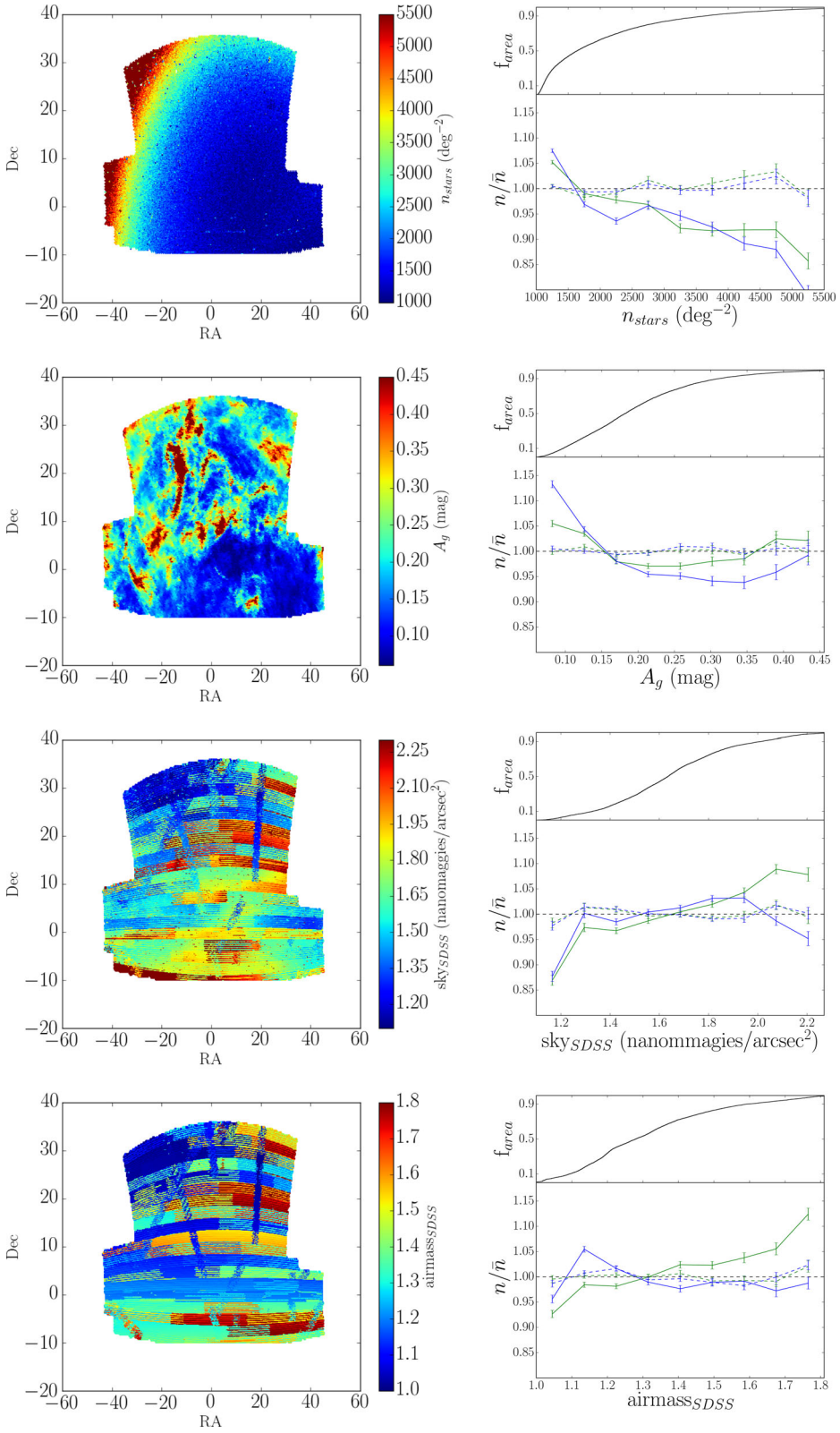

Figure 3. Maps of the observational parameters (left) and evolution of the normalized average number density ($n/\bar{n}$) as a function of each observational parameter (right). In each panel on the right, the top curve shows the fractional area of the survey which has a value of the parameter lower than or equal to the x-axis value. In the bottom panels, the solid lines correspond to the uncorrected density fluctuations, while the dashed curves represent the fluctuations remaining after applying the weights defined in Section 4.4. Blue curves are for the *UgrizW* selection and green curves for the *griW* selection. From top to bottom, the observational parameters correspond to the stellar density of stars with $18 < g < 21$, the Galactic extinction in g band (A_g), SDSS sky flux (sky$_{\rm SDSS}$) and SDSS airmass (airmass$_{\rm SDSS}$).

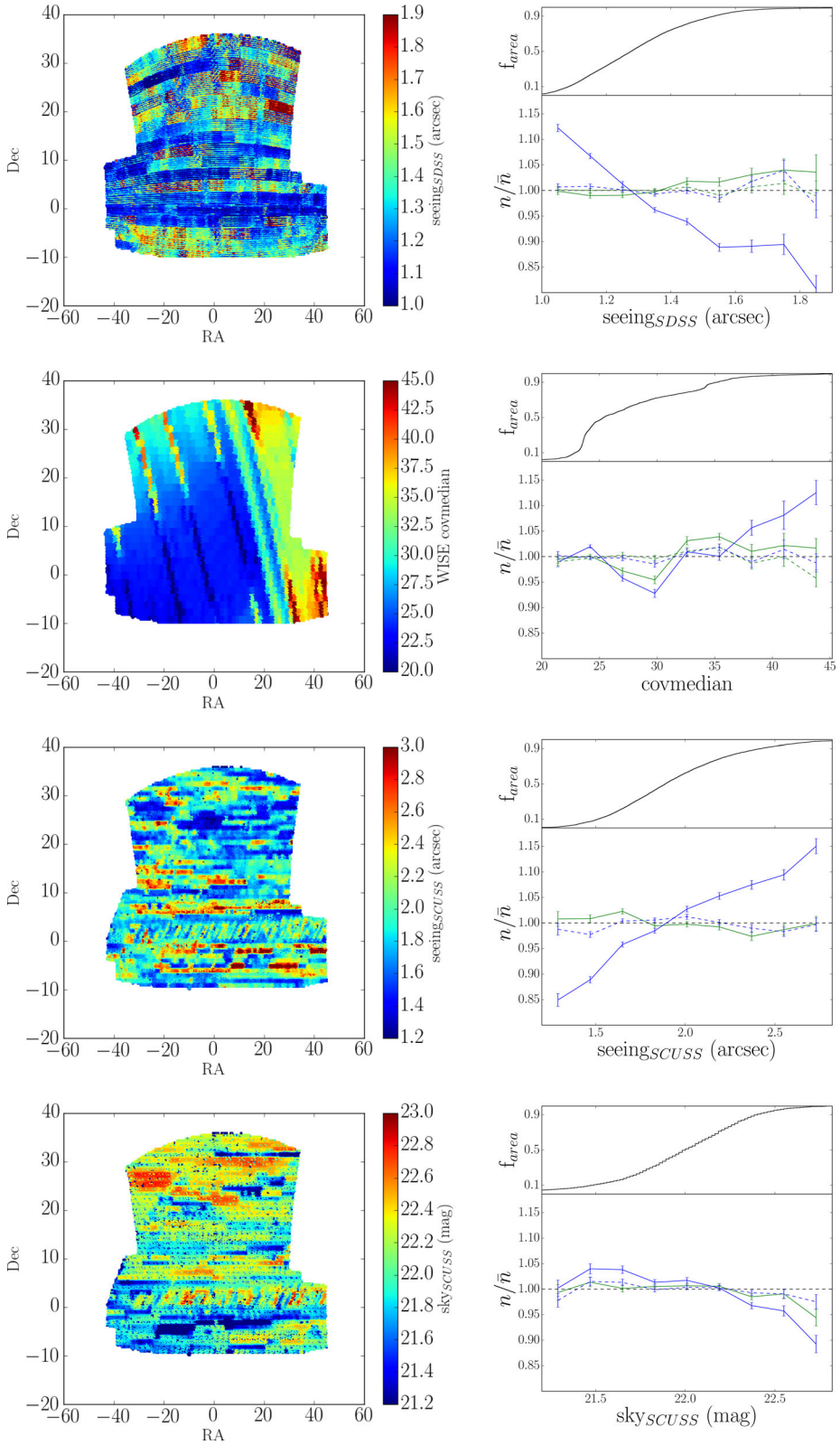

Figure 4. Same as Fig. 3 but for four different observational parameters: SDSS seeing (seeing$_{\rm SDSS}$), *WISE W*1 median coverage (covmedian), SCUSS seeing (seeing$_{\rm SCUSS}$) and SCUSS sky flux (sky$_{\rm SCUSS}$).

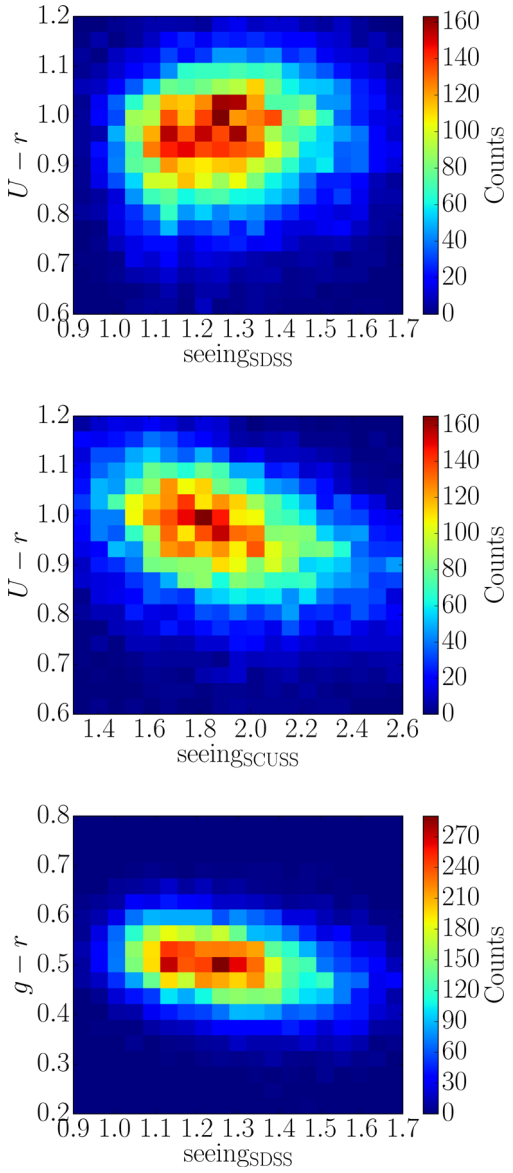

Figure 5. Two-dimensional histograms showing the distribution of the pixels of the *UgrizW* selection as a function of the mean values of the $U-r$ colour and of the seeing$_{\rm SDSS}$ (top panel) or seeing$_{\rm SCUSS}$ (middle panel) in the pixel. The correlations between the colour and the values of the seeings are clearly visible. For comparison, we also present the distribution of the pixels of the *UgrizW* selection as a function of the $g-r$ colour and of the seeing$_{\rm SDSS}$ (bottom panel) which shows very few correlations.

4.2 Foreground stars

To quantify the area masked by each star in our star sample, we estimate the number density of objects in our selections in annuli of different radii and of 1 arcsec width surrounding stars in our masked stellar map. We then obtain the mean number density around stars by averaging over all the stars in our sample. The resulting number density, normalized to the mean number density of our selection as a function of the radius of the annulus, is displayed in Fig. 6 for the *griW* selection. There is a clear deficit of targets surrounding stars at separations below 8 arcsec, while above that radius the number of targets surrounding stars is consistent with the average

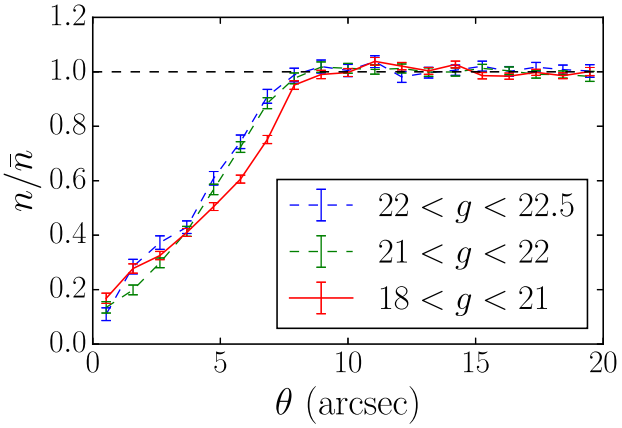

Figure 6. Number density of the *griW* selection normalized to the average number density of the selection in annuli of 1 arcsec width centred around stars as a function of the radius of the annulus. Our star sample corresponds to the $18 < g < 21$ curve. For comparison, we also plot the curves for samples selected in the same manner as our stellar sample but with $21 < g < 22$ and $22 < g < 22.5$. For each sample, there is a clear decrement of targets for radii below 8 arcsec.

of the selection. We compute the effective area masked by each star $\mathcal{A}_{\rm masked}$ as

$$\mathcal{A}_{\rm masked} = \int 2\pi \left(1 - \frac{n}{\bar{n}}\right) \theta {\rm d}\theta, \tag{2}$$

where θ is the radius of the annulus and $n/\bar{n}$ is taken from Fig. 6. We obtain $\mathcal{A}_{\rm masked} = 78.0$ arcsec^2 for the *griW* selection and $\mathcal{A}_{\rm masked} = 100.1$ arcsec^2 for the *UgrizW* selection.

Given a complete and pure sample of stars which mask a part of our footprint, we could compensate for this effect by correcting the number densities of the selections in each pixel given the stellar density in the pixel. As we select only bright ($18 < g < 21$) point sources, we are confident that the purity of our stellar sample is high. However, Fig. 6 shows that point sources with $21 < g < 22$ and $22 < g < 22.5$ mask a similar area of the sky as stars of our stellar sample. Selecting point sources at magnitude 22 and fainter is not a satisfactory approach to construct a pure stellar sample as the contamination by non-extended galaxies becomes non-negligible. Thus, we do not apply the correction and proceed by modelling the dependence on the stellar density of our selections, together with other parameters, as described in the next section.

4.3 Modelling the systematic effects

We follow the procedure of Prakash et al. (2016) to model the effect of the observational parameters on the number density of the selections. We assume that the observed number density in pixel p can be expressed as a function of all the parameters by

$$n_p = \bar{n} \left[1 + \sum_i \sum_k a_i^k \left(\frac{s_p^i - \tilde{s}_i}{\Delta s_i}\right)^k\right] + \epsilon_p, \tag{3}$$

where $\bar{n}$ corresponds to the average number density, s_i is the value of the parameter i, $\tilde{s}_i$ is the median value of the parameter i over the footprint, $\Delta s_i = \max(s_i) - \min(s_i)$ and ϵ_p is a term accounting for shot noise and cosmic variance. We have assumed that the effect of each parameter i on the observed number density can be modelled as a polynomial function of the value of the parameter with coefficients a_i^k, and that the shot noise and cosmic variance are Gaussian. The shot noise assumption is ensured by the fact that

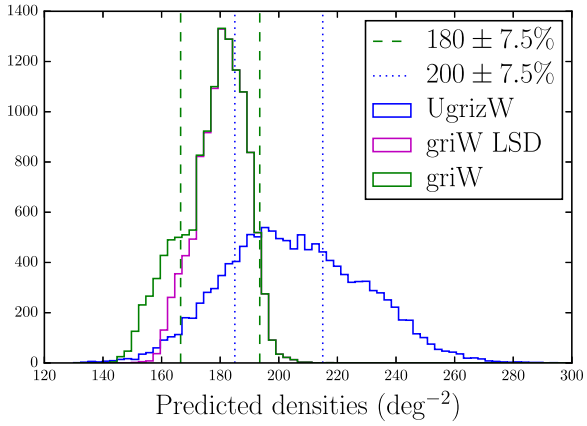

Figure 7. Distribution of the pixel densities for both selections. The *griW* selection is much more homogeneous than the *UgrizW* one. For indication, we trace two regions corresponding to fluctuations of ±7.5 per cent around 180 and 200 deg^{-2}, which is the total variation allowed by the requirements of Section 2. The mean densities of 180 and 200 deg^{-2} are somewhat arbitrary but roughly correspond to the peaks of the two distributions. For the peculiar case of the *griW* selection, we also plot as dotted line the distribution when only considering low stellar density (LSD) regions (defined as $n_{\rm stars} < 3000$) showing that the entire low-density tail is due to high stellar density regions.

we use sufficiently wide pixels such that the mean number of entry per pixel is ≈37 for the *griW* selection and ≈42 for the *UgrizW* one. We estimate the value of all coefficients a_i^k using a multivariate regression. The a_i^0 parameters are degenerate and therefore set to 0. For each observational parameter, we limit ourselves to first- ($k = 1$) or second-order ($k \leq 2$) polynomial depending on whether the density shows obvious non-linear dependence on the parameter. The orders of the polynomials fitted for the different parameters are listed in Table 2.

Knowing the value of the different observational parameters for each pixel, we can compute a predicted density per pixel

$$n_p^{\rm pred} = \bar{n}\left[1 + \sum_i \sum_k a_i^k \left(\frac{s_p^i - \tilde{s}_i}{\Delta s_i}\right)^k\right], \quad (4)$$

where, compared to equation (3), we have now removed the shot noise and cosmic variance. The middle panels of Fig. 2 show the predicted density maps for the two selections. As expected, the predicted density maps exhibit some of the characteristics of the dominant maps of the observational parameters. For instance, the unmasked high-extinction region near RA of −30° and Dec of −2° creates an overdensity of targets in both selections. Also visible on the *griW* predicted density map is a general trend of having lower densities at lower RA corresponding to an increase in stellar density as we approach the Galactic plane. The large stripes resulting from the SDSS time-delay imaging strategy, visible on the sky$_{\rm SDSS}$ map, are also present on the predicted density maps, while the patchy structure of the seeing$_{\rm SCUSS}$ map appears on the *UgrizW* predicted density map.

The distribution of the pixel densities is visible in Fig. 7. The distribution corresponding to the *griW* selection is much narrower than that of the *UgrizW* selection, which shows that this latter selection is more impacted by systematic effects. We emphasize on two regions corresponding to a ±7.5 per cent fluctuation around 180 and 200 deg^{-2}, respectively. The choice of the central values is somewhat arbitrary, but they roughly correspond to the maximum of the distribution of the two selections, i.e. they are close to maximizing the surface of the footprint passing the homogeneity requirement stated in Section 2. With these central values, 2121 deg^2 of the *griW* map pass the homogeneity requirement, whereas only 1242 deg^2 of the *UgrizW* selection do. Thus, it is possible to define a 1500 deg^2 footprint passing the requirements using the *griW* selection but not the *UgrizW* one. The tail of the distribution of the *griW* selection in Fig. 7 towards the low densities is only due to the masking effect of stars studied in Section 4.2; it can simply be removed by applying a tighter cut on the stellar density such as $n_{\rm stars} < 3000$.

4.4 Correcting for systematic effects

We have investigated the effects of six observational parameters on the *griW* selection and eight on the *UgrizW* selection. We have identified that the major source of potential systematic effects for both selections arises from the stellar density, sky$_{\rm SDSS}$ and the extinction A_g, whereas the *UgrizW* selection is also affected by both SDSS and SCUSS seeings. To limit the influence of those observational parameters, we have removed a small portion of the footprint which contains the most extreme values of the parameters.

As shown by ROSS11, we can further reduce the effect of those observational parameters by defining an appropriate weighting procedure. Given equation (3), an obvious expression for the weights is given by

$$w_p = 1 + \frac{\bar{n} - n_p^{\rm pred}}{n_p}. \quad (5)$$

Applying those weights to the pixel densities reduces the systematic effects, as shown in Figs 3 and 4, where the fluctuations of the reduced average number density are now consistent with zero given the uncertainties computed as the root mean square (rms) in the bin.

4.5 Zero-point fluctuations

The requirements of Section 2 also state that the number density of the selection should not vary by more than 15 per cent over the footprint as a function of imaging zero-points. As in Myers et al. (2015) and Prakash et al. (2016), we test this requirement by adding ±0.01 mag to each photometric band used and then rerunning the target selection algorithm to estimate the change in target density. We test each photometric band individually. The normalized change in target density due to the shift of a given band ($\frac{1}{N}\frac{\Delta N}{\Delta m}$) is then multiplied by the expected rms error in the photometric calibration of that band to obtain the expected rms variation in target density due to shifts of the imaging zero-point. We use the 1σ error estimates of Finkbeiner et al. (2016) for the SDSS bands (summarized in Table 3) and estimate a 1σ error of 0.016 for *W*1 from Jarrett et al. (2011). We adopt a SCUSS zero-point 1σ error of the order of 22 mmag from private communication with the SCUSS collaboration.

Assuming Gaussian errors, 95 per cent of our footprint lies within a ±2σ variation from the expected zero-point of any given photometric band, meaning that 95 per cent of our footprint has a variation in target number density lower than $4 \times \sigma_{\rm zp} \times \frac{1}{N}\frac{\Delta N}{\Delta m}$, where $\sigma_{\rm zp}$ is the rms error on the zero-point in the relevant photometric band. The resulting fluctuations for each photometric band are given in Table 3. The strongest fluctuations are obtained with SCUSS *U* band and SDSS *r* band on the *UgrizW* selection. However, those fluctuations are below 10 per cent over 95 per cent of the footprint, below the 15 per cent requirements. For the *griW* selection, the dominant fluctuations are due to *g* band and *r* band with 13 per cent and

Table 3. The impact of fluctuations in imaging zero-points on the number densities of the selections. The *Error* column lists the estimated 1σ error on the zero-point for the different photometric bands in mmag. For each selection, the first column corresponds to the normalized variation in number density due to a variation of the zero-point Δm, while the second column gives the resulting variation of number density in per cent over 95 per cent of the footprint.

Photometric band	Error (mmag)	*UgrizW* $\frac{1}{N}\frac{\Delta N}{\Delta m}$	*UgrizW* fluctuation (%)	*griW* $\frac{1}{N}\frac{\Delta N}{\Delta m}$	*griW* fluctuation (%)
SCUSS *U*	22	−1.1	9.4	–	–
SDSS *g*	9	−2.4	8.6	−3.6	13
SDSS *r*	7	3.5	9.8	4.3	12
SDSS *i*	7	−0.7	1.9	−1.7	4.8
SDSS *z*	8	−0.3	1.0	–	–
WISE W1	16	−1.1	7.3	−1.2	7.8

12 per cent, respectively. Thus, both selections are robust against variation of the imaging zero-points.

5 LARGE-SCALE ANGULAR CLUSTERING OF PIXELS

5.1 Method and model

Following Scranton et al. (2002) and ROSS11, we start by computing the angular clustering directly using the pixels defined in the previous section. For each pixel p, we define the galaxy overdensity as

$$\delta_p^g = \frac{n_p}{\bar{n}} - 1, \tag{6}$$

where n_p is the number density of galaxies in the pixel and $\bar{n}$ the mean number density over all the pixels. We also compute the fluctuations with respect to the mean for each observational parameter s_i as

$$\delta_p^{s_i} = \frac{s_p^i}{\bar{s}_i} - 1, \tag{7}$$

where s_p^i is the value of the observational parameter i in the pixel p and $\bar{s}_i$ is the mean value of the parameter over all the pixels. We can therefore compute the correlation function as

$$w(\theta) = \frac{\sum_{p,q} \delta_p^\alpha \delta_q^\beta \Theta_{p,q}}{\sum_{p,q} \Theta_{p,q}}, \tag{8}$$

where $\Theta_{p,q}$ equals 1 if the angular separation between pixels p and q falls into the angular bin θ and zero otherwise, and α and β denote either the galaxy overdensity g or an observational parameter s_i. Thus, the previous equation corresponds to an autocorrelation in the case $\alpha = \beta$, and a cross-correlation in the case $\alpha \neq \beta$. Computing the angular clustering directly with the pixels has the advantages of being much faster than doing the full computation with the individual galaxies and does not require the use of randoms as we are dealing with continuous fields. We are limited by the resolution of the pixels $\theta_{\rm pix} \sim 0.46$ deg.

We compute the errors on the angular clustering using a jackknife estimator (see e.g. ROSS11)

$$\sigma^2_{\rm Jack}(\theta) = \frac{N_{\rm s} - 1}{N_{\rm s}} \sum_{i=1}^{N_{\rm s}} [w(\theta) - w_i(\theta)]^2, \tag{9}$$

where $N_{\rm s}$ is the number of subsamples, w is the angular correlation over the full sample and w_i is the angular correlation over the subsample i. We divide our masked footprint into 24 equal-area subsamples by searching for continuous regions of neighbouring pixels with surface of $\mathcal{A}_{\rm tot}/N_{\rm s}$, where $\mathcal{A}_{\rm tot}$ is the area of the total footprint.

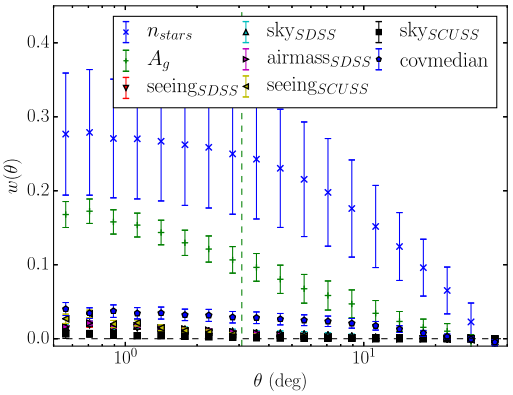

Figure 8. Autocorrelation of the eight observational parameters considered. The parameters with the strongest signals are the stellar density and the extinction A_g; thus, they are the most likely to induce errors on the clustering measurement. The signals in airmass, sky$_{\rm SDSS}$, seeing$_{\rm SDSS}$ and seeing$_{\rm SCUSS}$ are comparable. The error bars are computed using a jackknife estimator. The vertical green dashed line corresponds to the expected apparent BAO scale at $z = 0.76$.

5.2 Measurements

Fig. 8 shows the autocorrelations of the different observational parameters we consider. Consistently with ROSS11, the strongest signal comes from the stellar density autocorrelation with a value of 0.23 ± 0.08 at an angular separation $\theta_{\rm BAO} = 3.0$ deg which corresponds to the expected BAO scale at redshift 0.8. The quoted error is the 1σ diagonal error on the correlation measurement. The second dominant signal is the extinction A_g which is about two times lower than the stellar density autocorrelation signal, with a value of 0.10 ± 0.02 at $\theta_{\rm BAO}$. All of the remaining observational parameters exhibit much lower signal; airmass, sky$_{\rm SDSS}$, seeing$_{\rm SDSS}$ and seeing$_{\rm SCUSS}$ have similar signals below 0.02 down to the pixel scale $\theta_{\rm pix}$, whereas *WISE* covmedian has a slightly stronger signal of 0.03 ± 0.008 at $\theta_{\rm BAO}$. The autocorrelation of sky$_{\rm SCUSS}$ has the smallest signal with an autocorrelation value of 0.002 ± 0.002 at the BAO scale.

The angular autocorrelation signal of the *UgrizW* selection is displayed in the top panel of Fig. 9.

The value of the autocorrelation is 0.015 ± 0.003 at $2\theta_{\rm pix}$ and 0.01 ± 0.003 at $\theta_{\rm BAO}$. The high amplitude at the BAO scale and above is an indication of the presence of systematic effects. Also visible in this panel is the cross-correlation signal between the selection density and the value of the observational parameters. The cross-correlations with the stellar density and the extinction are larger with respective signals of -0.031 ± 0.01 and -0.021 ± 0.007 at the BAO scale. The negative signs are consistent with the negative slopes of the curves showing the evolution of the normalized number densities of the selection as a function of the parameters shown in Fig. 3. The next two cross-correlations with the most signal are those involving SCUSS and SDSS seeing, with respective signals of 0.01 ± 0.002 and -0.01 ± 0.001 on the pixel scale, and smaller signals of 0.004 ± 0.002 and -0.005 ± 0.001 at the BAO scale. Again the signs of the cross-correlations (i.e. positive with SCUSS seeing and negative with SDSS seeing) are consistent with

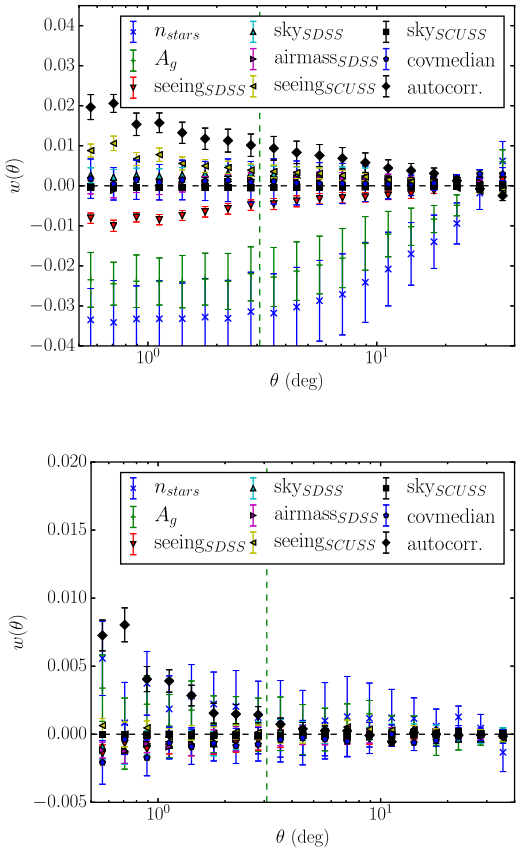

Figure 9. Top: auto-correlation of the galaxy density and cross-correlations between *UgrizW* selection galaxy density and the different observational parameters. Bottom: same format after applying the weighting technique. The vertical green dashed line corresponds to the expected apparent BAO scale at $z = 0.76$.

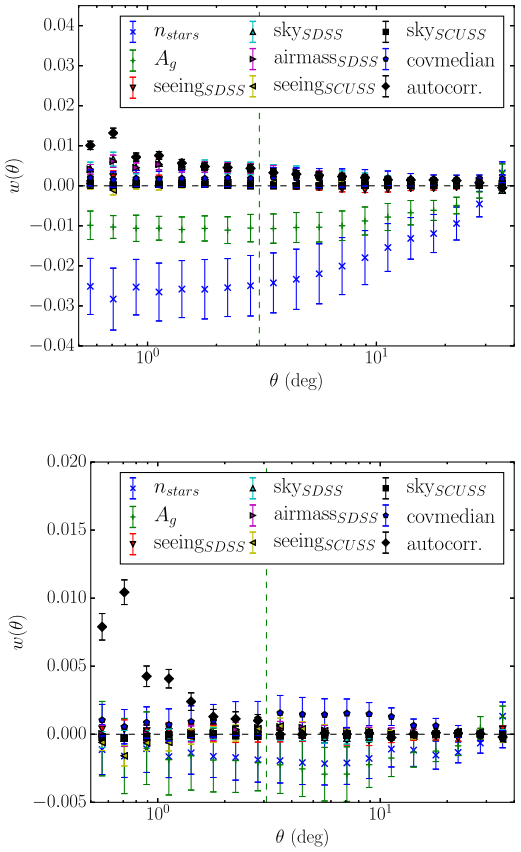

Figure 10. Top: auto-correlation of the galaxy density and cross-correlations between *griW* selection galaxy density and the different observational parameters. Bottom: same format after applying the weighting technique. The vertical green dashed line corresponds to the expected apparent BAO scale at $z = 0.76$.

the trends seen in Fig. 4. All other observational parameters have a cross-correlation with the selection density below 0.003 in absolute value over the full range of scales.

The bottom panel of Fig. 9 presents the angular autocorrelation function of the *UgrizW* selection density as well as the angular cross-correlations with the observational parameters when applying the correction weights defined in equation (5). The weighted autocorrelation has a signal of 0.004 ± 0.001 at twice the pixel scale, a third of the value of the unweighted autocorrelation. The value at the BAO scale is $(1.5 \pm 6) \times 10^{-4}$, and the autocorrelation is compatible with zero above the BAO scale, indicating that systematic errors have been removed. This result is confirmed by the cross-correlation measurements, which are now all within 1σ of zero for separations greater than two pixels. This is a reduction of a factor of 30 for the signal of the cross-correlation with the stellar density at the BAO scale, which is now 0.001 ± 0.003.

The angular autocorrelation signal of the *griW* selection is presented in the top panel of Fig. 10, together with the cross-correlations between the selection density and the observational parameters. As for the *UgrizW* selection, the angular correlation function has a high amplitude up to a separation of 20°, again indicating the presence of systematic errors. The value of the autocorrelation is 0.007 ± 0.001 at $2\theta_{\rm pix}$ and 0.004 ± 0.001 at $\theta_{\rm BAO}$. The cross-correlation with the stellar density is again the one having the largest signal with a value of -0.25 ± 0.008 at the BAO scale, slightly smaller than the cross-correlation between the stellar density and the *UgrizW* selection density. The cross-correlation with the extinction has a value of -0.01 ± 0.003 at $\theta_{\rm BAO}$, roughly half of the cross-correlation between the extinction and the *UgrizW* selection density. The two cross-correlations with the next higher signals are the ones with the airmass and sky$_{\rm SDSS}$, which both have a signal of 0.004 ± 0.001 at the BAO scale. The cross-correlations with the remaining observational parameters are all below 0.002 in absolute value at all separations.

The bottom panel of Fig. 10 shows the angular auto and cross-correlation functions for the *griW* selection when applying the correction weights. As for the *UgrizW*, there is a drastic improvement of the angular autocorrelation of the selection density, which now is $(4 \pm 0.7) \times 10^{-3}$ at twice the pixel scale. The value at the BAO scale is $0.001 \pm 4 \times 10^{-4}$, and the autocorrelation function is consistent with zero above that scale. As for the *UgrizW* selection, the cross-correlation signals have been drastically suppressed through the stellar density; the extinction and covmedian stand roughly 1σ away from zero.

Fig. 11 compares the two weighted angular autocorrelation functions of the *UgrizW* and *griW* selections. Although the two selections have different dependences on the observational parameters and different unweighted angular autocorrelation functions, the weighted autocorrelations are in good agreement up to the BAO scale. This result indicates that the two selections select similar populations of ELGs.

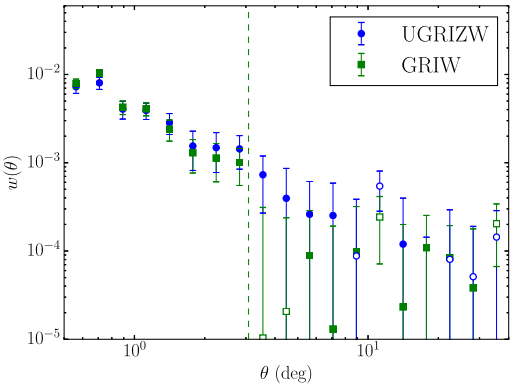

Figure 11. Comparison between the *UgrizW* selection galaxy density autocorrelation and the *griW* selection one. The vertical green dashed line corresponds to the expected apparent BAO scale at $z = 0.76$.

6 SMALL-SCALE ANGULAR CLUSTERING OF GALAXIES

6.1 Model

To model the small-scale angular clustering of our catalogues, we start with the matter power spectrum P obtained using CAMB[16] (Lewis, Challinor & Lasenby 2000) and the cosmological parameters defined in Section 1. When specified, we include non-linearities using the HALOFIT model (Takahashi et al. 2012). We compute the galaxy distribution power spectrum as

$$P_g(k, z) = b_g(z)^2 D_a(z)^2 P(k), \tag{10}$$

where D_a is the linear growth rate and b_g the bias of our galaxy sample. We compute the angular correlation function $w(\theta)$ as an integral of the power spectrum (e.g. Dodelson et al. 2002)

$$w(\theta) = \int \mathrm{d}k k^2 P(k) W_\theta(k), \tag{11}$$

where W_θ is the window function defined as

$$W_\theta(k) = \frac{1}{2\pi} \int \mathrm{d}r J_0(kr\theta) n^2(r), \tag{12}$$

J_0 is the Bessel function, r is the comoving distance and $n(r)$ is the normalized redshift distribution as a function of r.

In practice, we compute P_g at the median redshifts of the catalogues given in R16, i.e. $z_{\rm med} = 0.76$ for the *griW* selection and $z_{\rm med} = 0.78$ for the *UgrizW* one. When computing P_g including the HALOFIT modelling of non-linearities (equation 10), we multiply the matter power spectrum by the cutoff function $\exp(-(0.7k)^2)$ to ensure numerical convergence of the integral. This cutoff does not impact scales greater than $\theta = 0.1$ deg. We use the spectroscopic redshift distributions from R16 to compute W_θ.

6.2 Measurements and bias estimates

We compute the small-scale angular clustering of the galaxies using the Landy–Szalay estimator (Landy & Szalay 1993)

$$w = \frac{DD + RR - 2DR}{RR}, \tag{13}$$

with and without correcting for the systematic weights. We obtain the covariance matrix using a jackknife over 128 subsamples of equal number of pairs. Thus, the covariance between $w(\theta_i)$ and $w(\theta_j)$ is given by

$$\sigma^2_{\rm Jack}(\theta_i, \theta_j) = \frac{N_{\rm s} - 1}{N_{\rm s}} \sum_{p=1}^{N_{\rm s}} \left[w(\theta_i) - w_p(\theta_i)\right] \left[w(\theta_j) - w_p(\theta_j)\right], \tag{14}$$

where $N_{\rm s}$ is the number of subsamples, $w(\theta_i)$ is the angular clustering measured over the full catalogue at separation θ_i and $w_p(\theta_j)$ is the angular clustering measured for the jackknife subsample p at separation θ_j. The resulting angular correlation functions for both the *griW* and the *UgrizW* selections are visible in Fig. 12. We see that the systematic weights remove some clustering at all scales, even lower than the pixel size.

Table 4. Best-fitting value of the galaxy bias b_g and corresponding reduced χ^2 for the two catalogues and for the model of Section 6.1 including HALOFIT non-linearities. The reduced χ^2 are for 19 degrees of freedom.

Selection	b_g	$\chi^2/N_{\rm dof}$
griW	2.00 ± 0.04	1.28
UgrizW	1.89 ± 0.05	1.07

To fit the data, we use the theoretical model of Section 6.1 including the non-linearities from HALOFIT, with b_g as the only free parameter. Although the galaxy bias depends on the redshift, we do not fit a parametric function for b_g but rather a single average value for each selection. We fit the measurements over the range $0.2 < \theta < 0.7$ deg. The lower bound ensures good modelling of the correlation function while the upper bound removes regions possibly contaminated by remaining systematics. The resulting best-fitting models are displayed in Fig. 12, whereas the best-fitting value of b_g together with the χ^2 of the fits are reported in Table 4. For both the *griW* and *UgrizW* catalogues, the resulting best-fitting models including HALOFIT non-linearities are in very good agreement with the measurements. We obtain a bias of $b_g = 2.00 \pm 0.04$ or $b_g(z) = 1.35/D_a(z)$ for the *griW* selection and $b_g = 1.89 \pm 0.05$ or $b_g(z) = 1.28/D_a(z)$ for the *UgrizW* one. These results are in agreement with the measurements of Comparat et al. (2013) who found a bias of 1.9 for a similar selection. The slightly higher bias of the *griW* selection seems to confirm the results of R16 who found that the *griW* cuts select slightly redder galaxies than the *UgrizW* ones, thus likely to occupy more massive haloes. However, we emphasize that the quoted uncertainties are purely statistical and do not include systematics errors which could mitigate the difference. As previously reported (see e.g. Crocce et al. 2016), the linear theory shows strong discrepancy with the measurements for $\theta < 0.1$ deg.

7 CONCLUSIONS

eBOSS will provide the first high-precision measurement of the BAO scale using ELGs as a tracer of the matter density field. To reach this goal, eBOSS must obtain spectra of 190 000 confirmed ELGs contained within a footprint of 1500 deg^2. We have defined two large-scale catalogues of ELGs selecting by a Fisher discriminant technique and covering more than 2800 deg^2 over the SGC. The first catalogue, designated *UgrizW*, uses the *g*, *r*, *i* and *z* photometric bands from the SDSS, the *U* band from SCUSS and the *W*1 band from *WISE*. The second catalogue, designated *griW*, only uses information from SDSS *g*, *r* and *i* photometric bands and *WISE W*1

[16] http://camb.info/

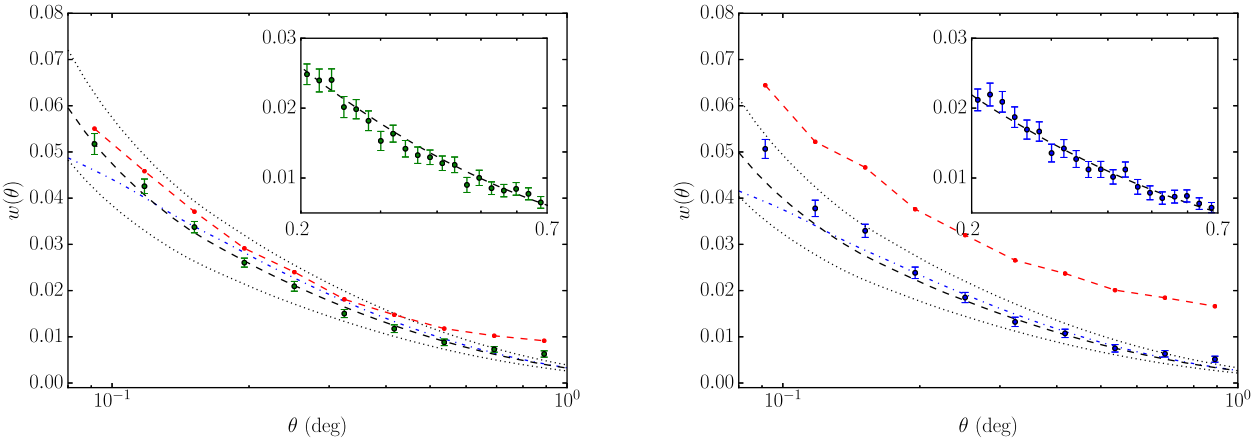

Figure 12. The angular correlation function of the *griW* (left) and *UgrizW* (right) catalogues computed on the discrete objects with the Landy–Szalay estimator. In each plot, we show the uncorrected correlation (red dots and dashed line), the corrected correlation (filled green/blue circles), the best-fitting model as computed in Section 6.1 with HALOFIT correction for the non-linearities (black dashed line) and without it (blue dash–dotted line) as well as two models corresponding to a galaxy bias $b_g = 1.8$ and 2.2 for the *griW* plot and $b_g = 1.7$ and 2.1 for the *UgrizW* plot, respectively (dotted black lines). The inset panels show a blow-up of the correlations over the fitting range $0.2 < \theta < 0.7$ showing the excellent agreement between the measurements and the models over that range.

band. R16 have verified that the selections meet the density, redshift distribution and purity requirements. In this paper, we focus on testing the homogeneity requirements.

We study the dependence of the angular number density of targets in the two selections as a function of observational parameters, including the stellar density, the Galactic extinction, SDSS sky flux, SDSS airmass, SDSS seeing, *WISE* median coverage, SCUSS seeing and SCUSS sky flux. The angular number densities of both selections depend substantially on the stellar density and the extinction. The correlation between the density of both selections and the stellar density is found to be negative, meaning that the larger the density of stars in the given field, the fewer objects are selected. We show that this effect can be understood as resulting from the low stellar contamination of our selections plus the fact that each star masks a small area $\mathcal{A}_{\rm masked}$ of the sky, preventing the selection of targets in that area. We estimate $\mathcal{A}_{\rm masked}$ to be on average 78.0 arcsec^2 for the *griW* selection and 100.1 arcsec^2 for the *UgrizW* selection. The angular number density of the *UgrizW* selection also depends strongly on both SDSS and SCUSS seeing. This behaviour results from a correlation between the $U - r$ colour term which enters the definition of the Fisher discriminant and those seeing parameters.

We model simultaneously the effect of every observational parameters using a multivariate regression which is quadratic as a function of the stellar density, the extinction and SDSS sky flux which exhibit explicit non-linear behaviour, and linear as a function of all other observational parameters. This modelling allows us to compute the predicted density of the selections in the absence of shot noise and cosmic variance given the value of the observational parameters.

The predicted density of the *griW* selection is contained within the ± 7.5 per cent variation (15 per cent total) as a function of the observational parameters, but the *UgrizW* selection is not, meaning that the *UgrizW* selection fails the homogeneity requirements of eBOSS. Based on our modelling, we propose a weighting procedure to remove the effect of the observational parameters on the number densities of both selections.

We study the variation in number density of our two selections as a function of variations in imaging zero-points, showing that both selections are within the requirements of eBOSS.

We compute the large-scale angular clustering of the two selections, showing that they both have excess of signal at and above the BAO scale indicating the presence of systematic errors in the measurements. We calculate the cross-correlation between our selections and the observational parameters. For both selections, the cross-correlation with the stellar density has the largest signal followed by the cross-correlation with the extinction. For the *UgrizW* selection, there are important cross-correlations with SDSS and SCUSS seeing, as expected from the previous results.

Our weighting procedure successfully removes the signal in the cross-correlations between the selections and the observational parameters which represents an improvement of a factor of 30 in the case of the stellar density.

We compute and model the small-scale angular clustering of the two catalogues in order to estimate the bias of the two selections. We find a bias of $1.35/D_a(z)$ for the *griW* selection and $1.28/D_a(z)$ for the *UgrizW* one.

Both catalogues are publicly available at https://data.sdss.org/sas/dr13/eboss/target/elg/fisher-selection/.

ACKNOWLEDGEMENTS

TD and JPK acknowledge support from the ERC advanced grant LIDA. JC acknowledges financial support from MINECO (Spain) under project number AYA2012-31101. AR acknowledges funding from the P2IO LabEx (ANR-10-LABX-0038) in the framework 'Investissements d' Avenir' (ANR-11-IDEX-0003-01) managed by the French National Research Agency (ANR). JC and FP acknowledge support from the Spanish MICINNs Consolider-Ingenio 2010 Programme under grant MultiDark CSD2009-00064, MINECO Centro de Excelencia Severo Ochoa Programme under grant SEV- 2012-0249 and MINECO grant AYA2014-60641-C2-1-P. EJ acknowledges financial support from CNRS/INSU, France.

Funding for SDSS-III has been provided by the Alfred P. Sloan Foundation, the Participating Institutions, the National Science Foundation and the US Department of Energy Office of Science. The SDSS-III website is http://www.sdss3.org/.

SDSS-III is managed by the Astrophysical Research Consortium for the Participating Institutions of the SDSS-III

Collaboration including the University of Arizona, the Brazilian Participation Group, Brookhaven National Laboratory, Carnegie Mellon University, University of Florida, the French Participation Group, the German Participation Group, Harvard University, the Instituto de Astrofisica de Canarias, the Michigan State/Notre Dame/JINA Participation Group, Johns Hopkins University, Lawrence Berkeley National Laboratory, Max Planck Institute for Astrophysics, Max Planck Institute for Extraterrestrial Physics, New Mexico State University, New York University, Ohio State University, Pennsylvania State University, University of Portsmouth, Princeton University, the Spanish Participation Group, University of Tokyo, University of Utah, Vanderbilt University, University of Virginia, University of Washington and Yale University.

Funding for the Sloan Digital Sky Survey IV has been provided by the Alfred P. Sloan Foundation, the US Department of Energy Office of Science and the Participating Institutions. SDSS-IV acknowledges support and resources from the Center for High-Performance Computing at the University of Utah. The SDSS website is www.sdss.org.

SDSS-IV is managed by the Astrophysical Research Consortium for the Participating Institutions of the SDSS Collaboration including the Brazilian Participation Group, the Carnegie Institution for Science, Carnegie Mellon University, the Chilean Participation Group, the French Participation Group, Harvard-Smithsonian Center for Astrophysics, Instituto de Astrofísica de Canarias, the Johns Hopkins University, Kavli Institute for the Physics and Mathematics of the Universe (IPMU)/University of Tokyo, Lawrence Berkeley National Laboratory, Leibniz Institut für Astrophysik Potsdam (AIP), Max-Planck-Institut für Astronomie (MPIA Heidelberg), Max-Planck-Institut für Astrophysik (MPA Garching), Max-Planck-Institut für Extraterrestrische Physik (MPE), National Astronomical Observatory of China, New Mexico State University, New York University, University of Notre Dame, Observatário Nacional/MCTI, the Ohio State University, Pennsylvania State University, Shanghai Astronomical Observatory, United Kingdom Participation Group, Universidad Nacional Autónoma de México, University of Arizona, University of Colorado Boulder, University of Portsmouth, University of Utah, University of Virginia, University of Washington, University of Wisconsin, Vanderbilt University and Yale University.

The SCUSS is funded by the Main Direction Program of Knowledge Innovation of Chinese Academy of Sciences (No. KJCX2-EW-T06). It is also an international cooperative project between National Astronomical Observatories, Chinese Academy of Sciences and Steward Observatory, University of Arizona, USA. Technical supports and observational assistances of the Bok telescope are provided by Steward Observatory. The project is managed by the National Astronomical Observatory of China and Shanghai Astronomical Observatory.

This publication makes use of data products from the *Wide-field Infrared Survey Explorer*, which is a joint project of the University of California, Los Angeles, and the Jet Propulsion Laboratory/California Institute of Technology, and NEOWISE, which is a project of the Jet Propulsion Laboratory/California Institute of Technology. *WISE* and NEOWISE are funded by the National Aeronautics and Space Administration.

REFERENCES

Anderson L. et al., 2014, MNRAS, 441, 24
Aubourg É. et al., 2015, Phys. Rev. D, 92, 123516
Betoule M. et al., 2014, A&A, 568, A22
Bolton A. S. et al., 2012, AJ, 144, 144
Cole S. et al., 2005, MNRAS, 362, 505
Colless M. et al., 2001, MNRAS, 328, 1039
Comparat J. et al., 2013, MNRAS, 433, 1146
Comparat J. et al., 2015, A&A, 575, A40
Comparat J. et al., 2016, A&A, 592, A121
Crocce M. et al., 2016, MNRAS, 455, 4301
Dawson K. S. et al., 2013, AJ, 145, 10
Dawson K. S. et al., 2016, AJ, 151, 44
de Jong R. S. et al., 2014, Proc. SPIE, 9147, 91470M
Delubac T. et al., 2015, A&A, 574, A59
Dodelson S. et al., 2002, ApJ, 572, 140
Eisenstein D. J. et al., 2005, ApJ, 633, 560
Eisenstein D. J. et al., 2011, AJ, 142, 72
Finkbeiner D. P. et al., 2016, ApJ, 822, 66
Fisher R. A., 1936, Ann. Eugenics, 7, 179
Font-Ribera A. et al., 2014, J. Cosmol. Astropart. Phys., 5, 27
Fukugita M., Ichikawa T., Gunn J. E., Doi M., Shimasaku K., Schneider D. P., 1996, AJ, 111, 1748
Gorski K. M., Wandelt B. D., Hansen F. K., Hivon E., Banday A. J., 1999, preprint (arXiv:e-prints)
Gunn J. E. et al., 1998, AJ, 116, 3040
Gunn J. E. et al., 2006, AJ, 131, 2332
Gwyn S. D. J., 2012, AJ, 143, 38
Ho S. et al., 2012, ApJ, 761, 14
Jarrett T. H. et al., 2011, ApJ, 735, 112
Landy S. D., Szalay A. S., 1993, ApJ, 412, 64
Lang D., Hogg D. W., Schlegel D. J., 2016, AJ, 151, 36
Laureijs R. et al., 2011, preprint (arXiv:1110.3193)
Levi M. et al., 2013, preprint (arXiv:1308.0847)
Lewis A., Challinor A., Lasenby A., 2000, ApJ, 538, 473
Lupton R. H., Gunn J. E., Szalay A. S., 1999, AJ, 118, 1406
Myers A. D. et al., 2006, ApJ, 638, 622
Myers A. D. et al., 2015, ApJS, 221, 27
Oke J. B., Gunn J. E., 1983, ApJ, 266, 713
Planck Collaboration XVI, 2014, A&A, 571, A16
Prakash A. et al., 2016, ApJS, 224, 34
Raichoor A. et al., 2016, A&A, 585, A50 (R16)
Ross A. J. et al., 2011, MNRAS, 417, 1350 (ROSS11)
Schlegel D. J., Finkbeiner D. P., Davis M., 1998, ApJ, 500, 525
Scranton R. et al., 2002, ApJ, 579, 48
Smee S. A. et al., 2013, AJ, 146, 32
Stoughton C. et al., 2002, AJ, 123, 485
Swanson M. E. C., Tegmark M., Hamilton A. J. S., Hill J. C., 2008, MNRAS, 387, 1391
Takada M. et al., 2014, PASJ, 66, 1
Takahashi R., Sato M., Nishimichi T., Taruya A., Oguri M., 2012, ApJ, 761, 152
Tojeiro R. et al., 2014, MNRAS, 440, 2222
Wright E. L. et al., 2010, AJ, 140, 1868
York D. G. et al., 2000, AJ, 120, 1579
Zhao G.-B. et al., 2016, MNRAS, 457, 2377
Zou H. et al., 2015, AJ, 150, 104
Zou H. et al., 2016, AJ, 151, 37

[1]*Laboratoire d'Astrophysique, Ecole Polytechnique Fédérale de Lausanne (EPFL), Observatoire de Sauverny, CH-1290 Versoix, Switzerland*
[2]*CEA, Centre de Saclay, IRFU/SPP, F-91191 Gif-sur-Yvette, France*
[3]*Instituto de Física Teórica, (UAM/CSIC), Universidad Autónoma de Madrid, Cantoblanco, E-28049 Madrid, Spain*
[4]*Departamento de Fisica Teorica, Universidad Autonoma de Madrid, Cantoblanco E-28049 Madrid, Spain*
[5]*Department of Physics and Astronomy, University College London, Gower Street, London WC1E 6BT, UK*
[6]*Aix Marseille University, CNRS, LAM, Laboratoire d'Astrophysique de Marseille, Marseille, France*

[7]*Key Laboratory of Optical Astronomy, National Astronomical Observatories, Chinese Academy of Sciences, Beijing 100012, China*
[8]*Department of Physics and Astronomy, University of Utah, Salt Lake City, UT 84112, USA*
[9]*Department of Physics & Electronics, Rhodes University, Grahamstown 6140, South Africa*
[10]*Department of Physics and Astronomy, University of Wyoming, Laramie, WY 82071, USA*
[11]*Department of Physics and Astronomy and PITT PACC, University of Pittsburgh, Pittsburgh, PA 15260, USA*
[12]*Institute of Cosmology & Gravitation, Dennis Sciama Building, University of Portsmouth, Portsmouth PO1 3FX, UK*
[13]*Institutode Astrofísica de Andalucía (CSIC),Glorieta de la Astronomía, E-18080 Granada, Spain*
[14]*Campus of International Excellence UAM+CSIC, Cantoblanco, E-28049 Madrid, Spain*
[15]*Center for Cosmology and Astroparticle Physics, Department of Physics, The Ohio State University, OH 43210, USA*
[16]*Department of Astronomy and Astrophysics, The Pennsylvania State University, University Park, PA 16802, USA*
[17]*Institute for Gravitation and the Cosmos, The Pennsylvania State University, University Park, PA 16802, USA*
[18]*Department of Physics & Astronomy, Johns Hopkins University, 3400 N. Charles Street, Baltimore, MD 21218, USA*

This paper has been typeset from a TEX/LATEX file prepared by the author.